Anisotropic quantum critical point in the Ce 3 Al system with a large magnetic anisotropy

S. Vrtnik, M Krnel, P. Kozelj, Z. Jaglicic, L Kelhar, A. Meden, Marie-Cécile de Weerd, Pascal Boulet, J. Ledieu, V. Fournee, et al.

Anisotropic quantum critical point in the Ce_3Al system with a large magnetic anisotropy

Journal of Physics Communications

PAPER

Anisotropic quantum critical point in the Ce_3Al system with a large magnetic anisotropy

S Vrtnik[1,2], M Krnel[1,2], P Koželj[1,3,2], Z Jagličić[4,2], L Kelhar[1,2], A Meden[5], M-C de Weerd[6,2], P Boulet[6,2], J Ledieu[6,2], V Fournée[6,2], J-M Dubois[6,2] and J Dolinšek[1,2,3]

[1] J. Stefan Institute, Jamova 39, SI-1000 Ljubljana, Slovenia
[2] International Associated Laboratory PACS2, CNRS and Université de Lorraine, Nancy–JSI, Ljubljana, Slovenia
[3] University of Ljubljana, Faculty of Mathematics and Physics, Jadranska 19, SI-1000 Ljubljana, Slovenia
[4] Institute of Mathematics, Physics and Mechanics and University of Ljubljana, Faculty of Civil and Geodetic Engineering, Jadranska 19, SI-1000 Ljubljana, Slovenia
[5] University of Ljubljana, Faculty of Chemistry and Chemical Technology, Večna pot 113, SI-1000 Ljubljana, Slovenia
[6] Institut Jean Lamour, UMR 7198 CNRS—Université de Lorraine, Campus Artem, 2 allée André Guinier, BP 50840, 54011 Nancy Cedex, France

E-mail: jani.dolinsek@ijs.si

Keywords: quantum critical point, quantum phase transition, Ce_3Al

OPEN ACCESS

RECEIVED
6 October 2020

REVISED
29 October 2020

ACCEPTED FOR PUBLICATION
3 November 2020

PUBLISHED
11 November 2020

Abstract

A magnetic field driven quantum critical point (QCP) is studied experimentally in the Ce_3Al magnetically anisotropic intermetallic compound, which shows both antiferromagnetic (AFM) ordering and heavy–fermion behavior. Measurements of the magnetic susceptibility, the magnetoresistance and the specific heat on a Ce_3Al monocrystalline sample performed down to 0.35 K in magnetic fields up to 9 T demonstrate that the QCP is anisotropic regarding the orientation of the magnetic field relative to the magnetically easy direction. External magnetic field drives the AFM transition continuously toward zero temperature when applied in the (a, b) easy plane, reaching the QCP at the critical field $B_c^{a,b} = 4.6 \pm 0.4$ T, where a quantum phase transition from the AFM to the paramagnetic state takes place. The magnetoresistance experiments below 1 K indicate that intermediate magnetic states may have formed near the QCP. For the field applied along the c hard direction, the QCP has not been observed within our experimental range of the magnetic field. The anisotropic, magnetic field driven QCP in the Ce_3Al results from competition of the exchange interaction with the Zeeman interaction in the presence of a large magnetocrystalline anisotropy. The anisotropy of the QCP is a consequence of the fact that the magnetic anisotropy locks the magnetization into the easy plane and cannot be pulled out of the plane by the available laboratory field. Consequently, only the component of the magnetic field vector that lies in the easy plane participates in the QCP formation. In AFM systems with a large magnetic anisotropy, the magnetic field driven QCP is a continuous variable of the magnetic field vector orientation relative to the easy direction.

1. Introduction

A quantum critical point (QCP) is a point in the phase diagram of a material where a continuous phase transition takes place at absolute zero temperature [1, 2]. Quantum phase transitions at $T = 0$ K are triggered by zero–point quantum fluctuations associated with Heisenberg's uncertainty principle, in contrast to conventional (thermodynamic) phase transitions that occur at a nonzero temperature and are triggered by thermal fluctuations. A QCP is typically achieved by a continuous suppression of a thermodynamic phase transition to zero temperature by the application of a magnetic field, pressure or through doping. Quantum phase transitions arise in quantum many–body systems because of competing interactions that foster different ground states. An example are the exchange interaction among the local moments that promotes magnetic ordering and the

Kondo exchange interaction between the local moments and the conduction electrons that favors a Kondo–screened singlet (nonmagnetic) ground state [3]. Another example are exchange–coupled spins in a transverse external magnetic field, where a continuous increase of the field can induce a quantum phase transition from a magnetically ordered state to a paramagnetic state via tuning the degree of quantum tunneling between the 'up' and 'down' spin–polarized states (the transverse–field Ising model). Prototype systems to explore QCPs are heavy–fermion (HF) metals, the most prominent examples being Ce– and Yb–containing compounds [4].

In magnetically anisotropic crystals, the magnetic moments tend to align with an easy axis, representing an energetically favorable direction of the magnetization in the crystal lattice. For certain lattices like hexagonal, an easy plane or an easy cone can also exist. In systems containing rare earth (RE) elements, the dominant source of magnetic anisotropy of the RE ions in a crystalline environment is the magnetocrystalline anisotropy. This anisotropy originates from the electrostatic interaction of the 4*f* electronic orbitals containing magnetic electrons with the electric field created by the rest of the crystal (the crystal field—CF). The CF interaction stabilizes a certain orbital, and by spin–orbit interaction the magnetic moment $\vec{\mu}$ is aligned in a particular crystallographic direction. The CF interaction is also able to reduce the size of the moments. The magnetocrystalline anisotropy may be so large that external magnetic fields $\vec{B} = \mu_0 \vec{H}$ up to hundreds of tesla are needed to overcome it by the Zeeman interaction $\mathcal{H}_z = -\vec{\mu} \cdot \vec{B}$. The CF interaction is a single–ion interaction, acting independently at each ionic site, and does not participate directly in the cooperative phenomena related to magnetic ordering.

A particular kind of a phase transition that can be driven to zero temperature by the magnetic field (leading to a QCP) occurs in anisotropic Néel–type antiferromagnets (AFM) with two equal and oppositely directed sublattice magnetizations $\vec{M}_A = -\vec{M}_B$, where the exchange interaction competes with the Zeeman interaction. For an uniaxial anisotropy, the AFM state with the field $\vec{H}$ perpendicular to the easy direction is more stable (energetically favorable) than the state with the field along the easy direction, owing to the fact that below the Néel temperature T_N, the perpendicular susceptibility $\chi_\perp$ is larger than the parallel susceptibility $\chi_\parallel$. When the field is applied along the easy direction, it tends to rotate the sublattice magnetizations perpendicular to the easy axis into a transverse, flopped configuration. According to the magnitude of the anisotropy energy, two cases may be distinguished. For a weak anisotropy, the two antiparallel sublattice magnetizations rotate suddenly at a critical (spin–flop) field H_{sf} perpendicular to the easy direction, hence perpendicular to the applied field. This is a spin–flop transition. Upon further increase of the field, $H > H_{sf}$, the two sublattice magnetizations continuously rotate into the field direction to form a saturated paramagnetic state with the spins polarized along the easy axis at $H \gg H_{sf}$. For a large anisotropy, the two sublattices remain polarized antiparallel along the easy direction up to the critical field H_{sf}, where the antiparallel sublattice suddenly rotates parallel to H, again forming the saturated paramagnetic state for $H > H_{sf}$. This is a spin–flip transition. The spin–flop and spin–flip transitions are both metamagnetic transitions, denoting a sudden increase of the magnetization upon a small change in the externally applied field. Low–temperature antiferromagnets with weak intrasublattice interactions usually undergo the spin–flip transition.

The spin–flop and spin–flip transitions are driven by the magnetic field as the control parameter and can occur at any temperature below T_N down to zero temperature. During the magnetic field sweep, the energy of the spin system is changing. At finite temperatures ($T > 0$), the energy conservation of the entire system (spins plus lattice) is maintained by thermal fluctuations, so that the transitions are thermodynamic. At $T = 0$, there are no thermal fluctuations anymore and the energy conservation is maintained by quantum fluctuations, so that the phase transitions become of a quantum nature, occurring at the QCP.

In multi–axially anisotropic AFMs, the situation is more involved. An example are hexagonal AFMs, where the hexagonal plane is either the easy plane (magnetically isotropic), or there exist six easy directions within the hexagonal plane with a small in–plane anisotropy. In both cases there exists a large anisotropy to the hard direction along the hexagonal axis perpendicular to the hexagonal plane. The QCP becomes anisotropic, depending on the direction of the magnetic field relative to the crystallographic axes and its experimental observation should necessarily be done on monocrystals. Here we report on the anisotropic QCP in the monoclinic (but very close to hexagonal) Ce_3Al compound that exhibits both the AFM ordering below $T_N \approx$ 2.6 K and the HF behavior.

2. Material description

Ce_3Al crystallizes at room temperature in a hexagonal structure (α–Ce_3Al) [5, 6], whereas at about 100 K, there is a structural transition to a monoclinic phase (γ–Ce_3Al), which is almost orthorhombic (the monoclinic angle amounts to $\gamma_m = 89.69°$). The monoclinic symmetry of the γ phase results from shifts of atoms within the mirror planes from their more symmetric positions in the α phase, so that the γ structure shows close similarity to the parent hexagonal α structure. Structural details of the α and γ phases, as well as their similarity are

discussed in the appendix A. The structure of the monoclinic γ phase can be viewed as consisting of slightly tilted Ce–Al and Ce–Ce chains that propagate along the *a* crystallographic direction and are alternately stacked along *b* and *c*.

Magnetic ordering in the Ce_3Al has been investigated before on polycrystalline samples [6–12]. Magnetically, there are two types of Ce ions in the structure. The Ce ions in the Ce–Al chains possess magnetic moments, which order AFM at $T_N \approx 2.6$ K, with the spins aligned antiparallel along the *a* chain direction. In contrast, there are no moments on the Ce–Ce chains at low temperatures due to Kondo compensation [8]. The crystal field splits the $J = 5/2$ line of Ce^{3+} into three doublets, where the two excited CF doublets occur at energies (in temperature units) $T_{CF1} \approx 75$ K and $T_{CF2} \approx 130$ K above the ground state doublet [9]. Crystal field strongly reduces the low–temperature saturated moment on the Ce–Al chains to 1.24 μ_B per Ce ion [8] (where μ_B is the Bohr magneton), as compared to the Ce^{3+} free–ion value of 2.5 μ_B. The electrical resistivity ρ is typical of a Kondo–lattice system, by exhibiting a Kondo resistance minimum at the temperature $T_K \approx 20$ K and a maximum at the Kondo lattice temperature $T^* \approx 3$ K, below which the resistivity strongly drops. The linear specific heat coefficient amounts to $\gamma = 95$ mJ/mol–CeK^2 [8], revealing that the effective mass of the electrons in the Ce_3Al is enhanced, but the electrons are not as heavy as in typical HF systems like $CeAl_3$ and UPt_3.

Our experiments were performed on a Ce_3Al monocrystal, grown by the Czochralski technique. Growth details, samples' description and structural characterization by XRD and electron microscopy are given in the appendix B.

3. Results

We have driven the AFM transition continuously towards zero temperature by the external magnetic field, monitored via the magnetic susceptibility, the magnetoresistance and the specific heat. Three sets of experiments were performed, with the magnetic field directed along the *a*, *b* and *c* crystal directions of the low–temperature monoclinic phase. In the following we label the anisotropic physical quantities with a superscript denoting the direction of the magnetic field (e.g., the magnetization M^a, the susceptibility χ^a, the resistivity ρ^a and the specific heat C^a for the field along *a*). Further experimental details are given in the appendix B.

3.1. Magnetic susceptibility

Direct current (dc) magnetic susceptibilities $\chi^{a,b,c} = M^{a,b,c}/H$ in the temperature range 300–1.9 K in a magnetic field $B = 0.1$ T are presented in figure 1(a), where a $1/T$–increase upon cooling, typical of localized moments, is evident. The positive, temperature–independent 'foot' originates mainly from the Pauli spin susceptibility, which is augmented due to the heavy effective mass of the charge carriers. The susceptibility is large and almost isotropic for the field applied in the (*a*, *b*) monoclinic plane ($\chi^a \approx \chi^b$), whereas the susceptibility for the field along *c* is much smaller, yielding the anisotropy $\chi^c \ll \chi^{a,b}$ at low temperatures. A small discontinuous step is observed at the $\alpha - \gamma$ structural phase transition, occurring at 98.5 K on cooling and at 101 K on heating. At $T_N = 2.6$ K, the AFM transition takes place ($\chi^{a,b,c}$ exhibit a maximum).

The AFM peak in the susceptibility shifts to lower temperatures with the increasing magnetic field, but the shift is anisotropic, depending on the field direction. The shift was studied by varying the field in small steps of $\Delta B = 0.2$ T from zero up to a 7–T field. In figure 1(b), the $\chi^{a,b,c}$ are shown zoomed in the temperature range of the AFM transition in three fields, $B = 0.1$, 3 and 5 T. For χ^a and χ^b, the peak in a 3–T field has moved significantly (and practically equally for both field directions) to a lower temperature, whereas in a 5–T field, the peak is no more observed down to the lowest measured temperature of 1.9 K. In contrast, the peak in χ^c almost did not shift with the field (inset in figure 1(b)). By defining the anisotropic, field–dependent Néel temperatures $T_N^{a,b,c}(B)$ (determined from the position of the highest point of the AFM peak, see arrows in figure 1(b)), we show this relation in figure 2(a). There is no significant anisotropy between $T_N^a(B)$ and $T_N^b(B)$, both decreasing strongly with the field, but there exists large anisotropy to $T_N^c(B)$, which shifts with the field very little.

The magnetization versus the magnetic field relation, $M^{a,b,c}(H)$, at $T = 2$ K is presented in the inset of figure 1(a). The $M^{a,b,c}$ all show a linear–like dependence on H, with the same anisotropy as the susceptibility, $M^c < M^a \approx M^b$. A slight increase of the slope can be noticed for the M^a and M^b (see the dashed guideline), happening at the field somewhere between 2 and 3 T. This is indicative of a field–induced phase transition from the AFM to a spin–flopped state, where both states are characterized by a linear $M(H)$ relation, but the slope is higher in the latter.

Based on the almost no in-plane anisotropy of the $\chi^{a,b}$ and $M^{a,b}$, the (*a*, *b*) monoclinic plane is close to the easy plane of the magnetization (see the discussion in the appendix B).

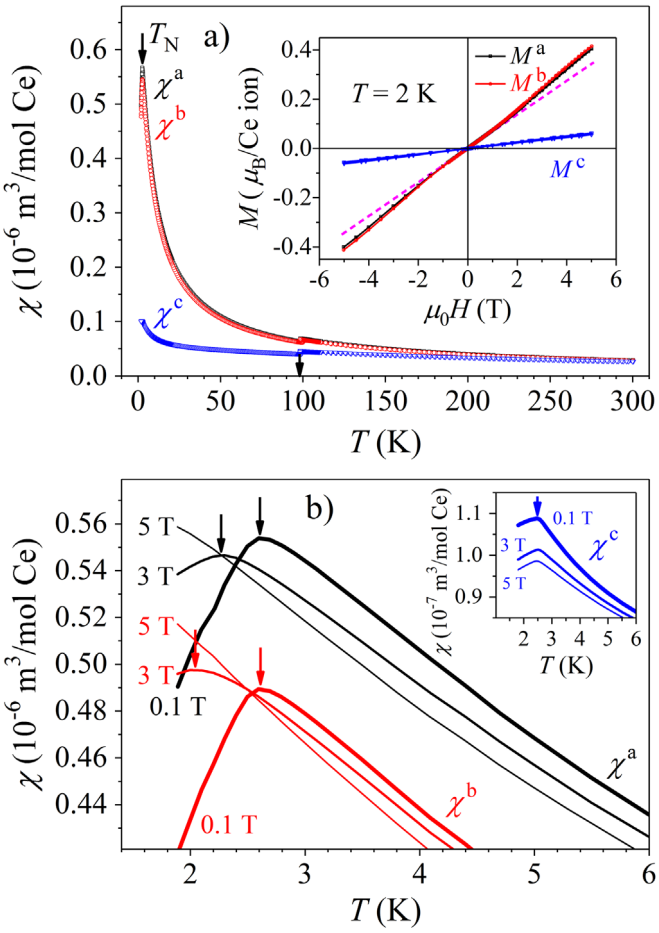

Figure 1. (a) Magnetic susceptibilities $\chi^{a,b,c}$ in a field $B = 0.1$ T. The arrow at $T \approx 100$ K marks the $\alpha - \gamma$ structural phase transition, whereas the arrow at $T_N = 2.6$ K marks the AFM transition. The $M^{a,b,c}(H)$ relation at $T = 2$ K is presented in the inset. Dashed line is a guide for the eye, demonstrating an increase of slope at a field somewhere between 2 and 3 T. (b) χ^a and χ^b in the temperature range of the AFM transition in selected fields $B = 0.1$, 3 and 5 T (for clarity of presentation, χ^b was shifted downwards by 0.07×10^{-6} m^3/mol Ce). The corresponding graph of χ^c is shown in the inset.

3.2. Magnetoresistance

The electrical resistivity and the magnetoresistance measurements were performed down to 0.35 K, with the current directed always along the *a* crystal direction (the direction of the Ce–Al chains). Since in a crystal of symmetry lower than cubic the resistivity is a tensor, this has assured that the same component of the resistivity tensor has always been measured (ρ_{xx}, abbreviated in the following as ρ). The resistivity in a magnetic field up to 9 T applied along the *a*, *b* and *c* (i.e., ρ^a, ρ^b and ρ^c) is presented in the appendix C. There is a small anisotropy between ρ^a and ρ^b, both being significantly affected by the field below the Kondo resistance minimum at $T_K \approx 23$ K (ρ^a and ρ^b in the field are reduced, but the Kondo minimum is preserved up to 9 T). In contrast, the resistivity ρ^c is much less affected by the field. The influence of magnetic ordering in the Ce–Al chains is best observed in the anisotropic magnetoresistance $[\rho^i(B) - \rho^i(0)]/\rho^i(0) = \Delta\rho^i/\rho^i$, $(i = a, b, c)$ which is shown in figure 3 at temperatures between 3 and 0.35 K in fields up to 9 T. Here it is important to stress that for the $\Delta\rho^a/\rho^a$, the current was parallel to the magnetic field, so that this is the longitudinal magnetoresistance, whereas for the $\Delta\rho^b/\rho^b$ and $\Delta\rho^c/\rho^c$, the current was perpendicular to the field, representing the transverse magnetoresistance. The longitudinal and transverse magnetoresistances usually do not differ much, typically up to about 3%. In figure 3, small anisotropy of the magnetoresistances $\Delta\rho^a/\rho^a$ and $\Delta\rho^b/\rho^b$ is observed for the field applied in the (*a*, *b*) plane, but there exists large anisotropy to $\Delta\rho^c/\rho^c$ for the field along *c*. At $T > T_N$ (in the paramagnetic phase), $\Delta\rho^a/\rho^a$ and $\Delta\rho^b/\rho^b$ are negative in the entire field range and approach linear variation at larger fields. This is the expected variation for paramagnetic (and also ferromagnetic) systems, originating from suppression of fluctuations of the localized spins by the magnetic field [13, 14], leading to a decrease of the resistivity. Below T_N, $\Delta\rho^a/\rho^a$ and $\Delta\rho^b/\rho^b$ are positive at low magnetic fields, increasing roughly as B^2 (parabolic fits of the 1.9-K curves are shown in figure C2 of the appendix C). At a 'critical' field, both magnetoresistances exhibit a maximum and then start to decrease for higher fields in the same manner as in the paramagnetic and ferromagnetic cases. The positions of the maxima $(\Delta\rho^a/\rho^a)_{max}$ and $(\Delta\rho^b/\rho^b)_{max}$ on the field axis (marked by vertical arrows in figures 3(a) and (b)) depend on the temperature and shift to higher fields at

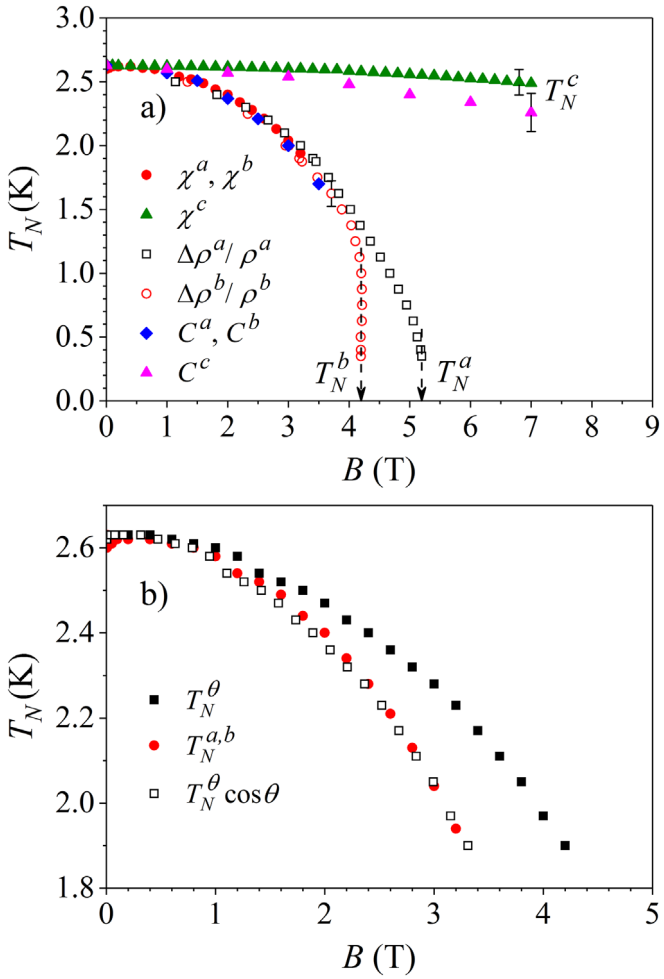

Figure 2. (a) The Néel temperatures $T_N^{a,b,c}(B)$, determined from the magnetic susceptibility, the magnetoresistance and the specific heat (the method is indicated in the legend). The origin of small discrepancy of the $T_N^c(B)$ data determined from χ^c and C^c is discussed in the appendix B. (b) The $T_N^{a,b}(B)$ values determined from χ^a and χ^b compared to the $T_N^\theta(B)$ values, obtained from the magnetic susceptibility with the magnetic field tilted by $\theta \approx 35°$ out of the (a, b) plane. The scaled data $T_N^\theta \cos\theta$ are also shown, overlapping perfectly with the $T_N^{a,b}(B)$ data.

lower temperatures. The magnetoresistances $\Delta\rho^a/\rho^a$ and $\Delta\rho^b/\rho^b$ are both large, reaching the maximum positive values $(\Delta\rho^a/\rho^a)_{\max} \approx 10\%$ and $(\Delta\rho^b/\rho^b)_{\max} \approx 13\%$ at $T = 0.75$ K. The relatively simple shape of the magnetoresistance curves at temperatures above 1 K that show a transition from a B^2 to a $-B$ dependence after passing a maximum becomes more complicated below 1 K, because some additional structure develops on both sides of the maximum (clearly evident when comparing the 1.9-K and 0.35-K curves in the insets of figures 3(a) and (b)). This structure is slightly different for $\Delta\rho^a/\rho^a$ and $\Delta\rho^b/\rho^b$, but the maximum remains well pronounced.

The shapes of the $\Delta\rho^a/\rho^a$ and $\Delta\rho^b/\rho^b$ curves at temperatures $T > 1$ K (where the additional structure around the maximum is still absent) can be explained by considering that the magnetic field induces a spin–flip type transition from the AFM to a paramagnetic state. For the field pointing along the magnetization direction of the two oppositely polarized spin sublattices of the AFM structure, the fluctuations of spins on the sublattice parallel to the field are suppressed in the same way as in the paramagnetic and ferromagnetic cases, whereas the fluctuations of spins on the antiparallel sublattice are increased (the field tries to turn over these spins). The total magnetoresistance in such a case is positive and increases as B^2 at low fields [14]. At the critical field, the spins of the antiparallel sublattice rotate into the field direction and the magnetoresistance starts to decrease roughly as $-B$ with the increasing field. The magnetoresistance thus exhibits a maximum at the critical field. The critical field value at a given temperature can be used to construct the field–dependent Néel temperature $T_N(B)$. The $T_N^a(B)$ and $T_N^b(B)$ values, obtained from the magnetoresistances $\Delta\rho^a/\rho^a$ and $\Delta\rho^b/\rho^b$, respectively, are also plotted in figure 2(a), confirming that there is no pronounced anisotropy for the field along a or b at

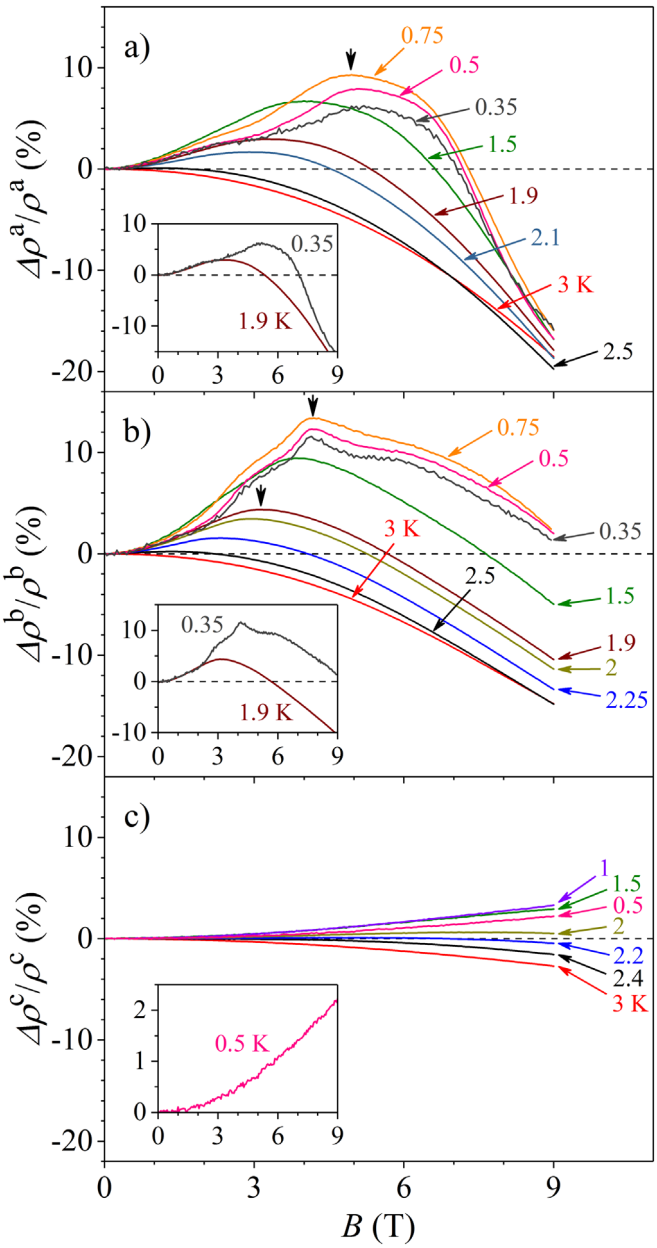

Figure 3. The anisotropic magnetoresistance (a) $\Delta\rho^a/\rho^a$, (b) $\Delta\rho^b/\rho^b$ and (c) $\Delta\rho^c/\rho^c$ at temperatures between 3 and 0.35 K in fields up to 9 T. Vertical arrows in panels (a) and (b) mark the magnetoresistance maxima for selected temperatures.

temperatures above 1 K, $T_N^a(B) \approx T_N^b(B)$. Good matching to the values obtained from the magnetic susceptibilities χ^a and χ^b is evident in the overlapping region.

At temperatures below 1 K, where the $\Delta\rho^a/\rho^a$ and $\Delta\rho^b/\rho^b$ curves show additional structure in the vicinity of the maximum, the $T_N^a(B)$ and $T_N^b(B)$ values no more coincide. While the $T_N^a(B)$ curve below 1 K shows smooth continuation of the trend from the temperatures above 1 K, the $T_N^b(B)$ curve does not change with the field anymore and becomes infinitely steep. This additional structure suggests that the magnetic field–temperature (B, T) phase diagram below 1 K in the region close to the critical magnetic field may involve intermediate magnetic phases between the simple collinear AFM and the paramagnetic phases, which depend on the field direction. Magnetic neutron scattering experiments within the critical region are needed to resolve this question.

The magnetoresistance $\Delta\rho^c/\rho^c$ (figure 3(c)) is very small as compared to $\Delta\rho^a/\rho^a$ and $\Delta\rho^b/\rho^b$. In the low–field regime $B < 2$ T, $\Delta\rho^c/\rho^c$ is practically zero at all investigated temperatures below 3 K. At higher fields, a weak field dependence develops (roughly as B^2, see the inset in figure 3(c)), but no pronounced maximum can be observed. The almost vanishing magnetoresistance $\Delta\rho^c/\rho^c$ can be explained by considering that the magnetic field applied along c now points perpendicular to the easy plane, hence perpendicular to the magnetization direction of the two oppositely polarized AFM spin sublattices. In the low–field region, this yields

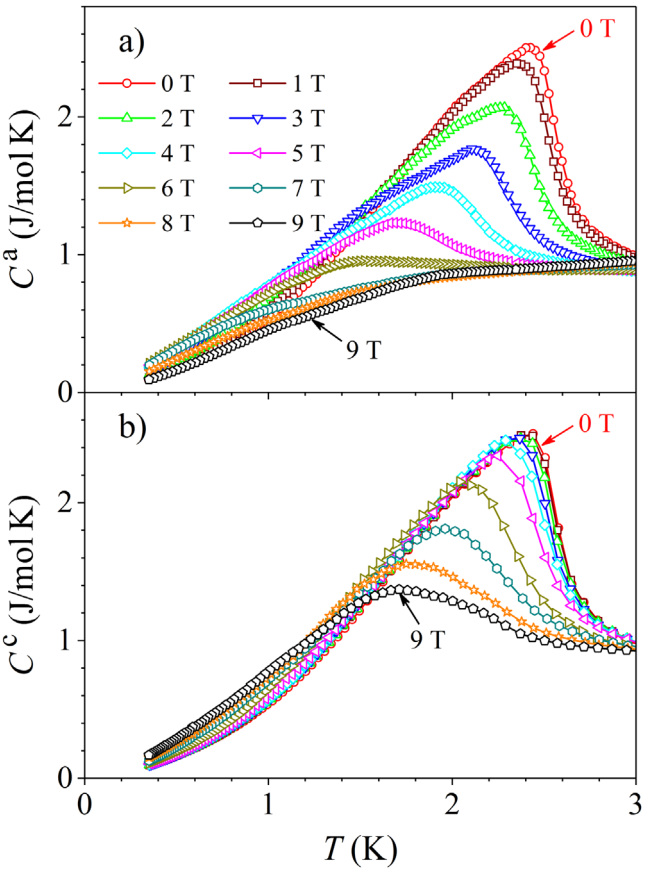

Figure 4. The anisotropic specific heat of Ce_3Al in the temperature range from 3 to 0.35 K in magnetic fields 0–9 T applied along (a) the *a* direction (C^a) and (b) the *c* direction (C^c).

zero magnetoresistance [14]. The strong anisotropy of the magnetoresistance, $\Delta\rho^c/\rho^c \ll \Delta\rho^{a,b}/\rho^{a,b}$ originates from the fact that the direction of the AFM magnetization in the crystal lattice is locked into the (*a*, *b*) monoclinic plane by the dominant CF interaction. External magnetic field within our accessible range up to 9 T is unable to change the orientation of the sublattice magnetizations relative to the *c* axis, but can easily rotate them within the (*a*, *b*) easy plane.

3.3. Specific heat

The field–induced shift of the AFM transition was monitored also via the specific heat. In magnetically anisotropic crystals, the magnetic specific heat in a magnetic field also becomes anisotropic, because the magnetic energy level scheme varies with the field direction. Anisotropic specific heat in a magnetic field is not unknown in literature and has been reported e.g. for the $CeCu_6$ Kondo–lattice system [15]. The anisotropic (total) specific heat of Ce_3Al in the temperature range from 3 to 0.35 K in magnetic fields 0–9 T is presented in figure 4.

No pronounced anisotropy was found for the field along *a* and *b* ($C^a \approx C^b$), so that only C^a and C^c are shown. For both field directions, a peak is observed at T_N due to the AFM ordering. The peak in C^a shifts strongly with the field to lower temperatures and decreases in height (figure 4(a)). At fields higher than about 5 T, no pronounced AFM peak can be observed in C^a anymore (the field has destroyed the AFM transition). For C^c (figure 4(b)), the shift of the AFM peak with the field is much weaker and the peak remains to be observed up to the highest field of 9 T (the AFM transition is not destroyed by the field along *c*). This is the same type of anisotropy as observed in the magnetic susceptibility.

The peak in the specific heat provides another means to determine the $T_N^{a,b,c}(B)$ relation. The T_N values determined from the specific heat were found systematically lower by 0.2 K as compared to the values determined from the magnetic susceptibility peak (i.e., the peak of the zero–field specific heat occurs at $T_N = 2.4$ K, whereas the low–field susceptibility peak occurs at $T_N \approx 2.6$ K). The origin of this small discrepancy is discussed in the appendix B. The $T_N^{a,b,c}(B)$ values shifted up by 0.2 K are also plotted in figure 2(a), where good matching to the values obtained from the magnetic susceptibility and the magnetoresistance is evident.

4. Discussion

The $T_N^a(B)$ and $T_N^b(B)$ data summarized in figure 2(a) demonstrate that the external magnetic field drives the AFM transition continuously toward zero temperature for the field applied in the (a, b) easy plane. The magnetoresistance data of figure 3 indicate that at temperatures above 1 K, the field–induced phase transition is of a spin–flip type from the AFM to the paramagnetic state, thermodynamic in nature. This kind of a phase transition is plausible, because Ce_3Al is a low–temperature antiferromagnet with weak intrasublattice interactions (as evidenced by the low $T_N(B = 0) \approx 2.6$ K). Since the phase transition temperature can be continuously driven toward zero, this suggests that at $T = 0$, the magnetic field can be used as a non–thermal control parameter to induce a quantum phase transition, and the critical field value B_c where the AFM state is destroyed represents the QCP. Extrapolating the $T_N^a(B)$ and $T_N^b(B)$ curves to $T = 0$, the QCP occurs at $B_c^a = 5.0$ T for the field along a and $B_c^b = 4.2$ T for the field along b. For the field applied along the perpendicular c (hard) direction, the QCP could not be observed within our experimental range of the magnetic field. The anisotropy of the QCP can be understood by considering that the two competing interactions are the indirect exchange and the Zeeman interaction, which compete in the presence of a much larger CF interaction that fixes the moments $\vec{\mu}$ into the easy plane. A simple estimate of the critical field value B_c can be obtained by equalizing the magnitudes of the exchange and the Zeeman interactions, where $E_{ex}/k_B \approx 2.6$ K (the zero–field Néel temperature), whereas $E_Z = 1.24\ \mu_B B$ (taking the moment μ value from [8]). The condition $E_{ex} = E_Z$ is fulfilled at $B_c = 3.1$ T, which matches qualitatively well to the experimental B_c^a and B_c^b values. A continuous increase of the magnetic field from 0 to 9 T thus tunes the magnitude of the Zeeman interaction from the condition $E_Z < E_{ex}$ to $E_Z > E_{ex}$, passing through the QCP at the critical field. For the magnetic field tilted by an angle θ out of the (a, b) easy plane, only the in–plane component of the magnetic field vector $B\ \cos\theta$ participates in the Zeeman interaction, a consequence of the fact that the magnetic field is unable to pull the magnetization out of the easy plane due to the large anisotropy to the c hard direction. For the field along c, $\theta = \pi/2$ and $\mathcal{H}_Z = 0$, so that the QCP does not occur within the accessible field range (as one of the two competing interactions is missing), whereas for the in–plane field application ($\theta = 0$), the QCP occurs at the lowest value of the magnetic field. For a general tilt of the field out of the (a, b) plane, the QCP should occur at a higher field, which scales with the tilt angle θ as $B_c(\theta) = B_c(0)/\cos\theta$. This consideration has been tested via the magnetic susceptibility, by tilting the magnetic field for $\theta \approx 35°$ out of the (a, b) plane and following the field–induced shift of the AFM peak in the upper temperature range of the AFM phase (down to 1.9 K). The raw data labeled as T_N^θ and the scaled data $T_N^\theta\ \cos\theta$ are presented in figure 2(b), where it is seen that the field dependence of $T_N^\theta(B)$ is considerably weaker than that of $T_N^{a,b}(B)$, whereas the scaled data $T_N^\theta\ \cos\theta$ perfectly overlap with the .

The critical fields B_c^a and B_c^b, determined by extrapolating the magnetoresistance data, are slightly different (5.0 T versus 4.2 T), but the difference is relatively small. In view of the in–plane isotropy of all other reported physical parameters (i.e., the (a, b) plane is very close to the easy plane) and uncertainties in the interpretation of the magnetoresistance (recall that $\Delta\rho^a/\rho^a$ is the longitudinal magnetoresistance, whereas $\Delta\rho^b/\rho^b$ is the transverse magnetoresistance), it appears plausible that both in–plane crystallographic directions have the same critical field for the transition to the intermediate and paramagnetic states. It is hence reasonable to assume a single in–plane critical field $B_c^{a,b} = 4.6 \pm 0.4$ T.

The temperature range below 1 K deserves special attention. Second–order phase transitions are marked by the growth of random fluctuations on ever–longer length scales, called 'critical fluctuations'. At the classical critical points, the critical thermal fluctuations are limited to a narrow region around the phase transition. For a quantum phase transition, on the other hand, the influence of quantum fluctuations is felt over a wide range of temperatures above the QCP, so that the effect of quantum criticality is felt to higher temperatures without ever reaching absolute zero. Quantum critical fluctuations dominate the physical properties of a metallic material also at nonzero temperatures and away from the critical magnetic field, within the quantum critical region. In response to the quantum critical fluctuations, the properties of a metal depart qualitatively from the standard Fermi–liquid behavior, to form a metallic state sometimes called a non–Fermi liquid or a 'strange metal'. Quantum critical fluctuations can also drive the formation of exotic magnetic phases in the vicinity of the QCP [16].

For the Ce_3Al, there is a twofold experimental evidence on the existence of a quantum critical region. The first is the electrical resistivity (presented in the appendix C), where the zero–field resistivity shows a T^2 dependence, compatible with a Fermi liquid, in the low–temperature region between the lowest measured temperature of 0.35 K up to $T \approx 1.7$ K (figure C1). Upon increasing the magnetic field applied in the (a, b) monoclinic plane, the temperature interval, where the resistivity shows a T^2 dependence, becomes progressively smaller (the upper limit of this interval shifts to lower temperatures), whereas for the field $B > 4$ T, no T^2 dependence is observed anymore (inset in figure C1(b)). This can be understood by considering that the

magnetic field within the quantum critical region above the QCP has destroyed the Fermi-liquid state. For the field applied along the *c* hard direction, the resistivity continues to show a T^2 dependence up to the highest field of 9 T (inset in figure C1(c)), which is consistent with the fact that no QCP is formed for the field in the *c* direction and the Fermi–liquid state is consequently not destroyed. The second evidence on the quantum critical region comes from the magnetoresistance (figure 3), where below about 1 K, the magnetoresistances $\Delta\rho^a/\rho^a$ and $\Delta\rho^b/\rho^b$ no longer show the relatively simple shape of a B^2 dependence at low fields that turns to a $-B$ dependence at high fields after passing a maximum at the spin–flip transition from the AFM to the paramagnetic state. The additional structure that develops on both sides of the magnetoresistance maxima (insets in figures 3(a) and (b)) suggests that novel magnetic phases could have formed within the quantum critical region. This effect is absent for the $\Delta\rho^c/\rho^c$, which is again consistent with the fact that no QCP is formed for the field in the *c* direction up to the highest available field of 9 T.

The Ce_3Al magnetic phase diagram and the $T_N^{a,b,c}(B)$ curves presented in figure 2(a) could be modeled in principle by taking into account that the AFM ordering of the Ce moments takes place on the Ce–Al chains, whereas the Ce moments of the Ce–Ce chains do not order because they are strongly reduced by the Kondo effect. Disregarding the Ce–Ce chains, the appropriate spin Hamiltonian for a Ce–Al chain would be a spin 5/2 Heisenberg antiferromagnet with exchange anisotropy of an XXZ–type and a quadratic single–ion CF anisotropy $D(S_z)^2$, in the presence of a magnetic field. This model has been widely investigated for spins 1/2 and 1 in two and three dimensions on square and cubic lattices [17, 18]. For a spin 5/2, numerical calculations appear to be unfeasible due to the size of the respective Hilbert space.

5. Conclusions

The anisotropic, magnetic field driven QCP in the Ce_3Al results from competition of the exchange interaction with the Zeeman interaction in the presence of a large magnetocrystalline anisotropy. External magnetic field applied within the easy plane drives the AFM transition continuously toward zero temperature, leading to a quantum phase transition from the AFM to the paramagnetic state at $T = 0$. The electrical resistivity and magnetoresistance experiments below 1 K indicate that intermediate magnetic states may have formed near the QCP. For the field along the hard direction, the AFM transition does not shift with the field and the QCP has not been observed within our experimental range of the magnetic field (up to 9 T). The large magnetocrystalline anisotropy locks the magnetization into the easy plane, which cannot be pulled out of the plane by the available laboratory field. Only the component of the magnetic field vector that lies in the plane participates in the Zeeman interaction, so that tilting the field out of the easy plane effectively tunes the magnitude of this interaction. In the AFM systems with a large magnetic anisotropy, the magnetic field driven QCP is generally anisotropic. The critical magnetic field $B_c(\theta)$ of the QCP is a continuous variable of the magnetic field vector orientation θ relative to the easy direction. As a technical remark, the observation of the anisotropic QCP in magnetically anisotropic systems should necessarily be performed on monocrystalline samples, with the magnetic field applied along well defined crystal directions.

Appendix A. Ce_3Al structural details

The room–temperature structure of Ce_3Al is hexagonal (α–Ce_3Al), space group $P6_3/mmc$ (No. 194), with unit cell parameters $a = 7.008$ Å and $c = 5.422$ Å [5]. There are two atomic sites in the unit cell, Ce (in 6 h Wyckoff position) and Al (2d). At about 100 K, there is a structural transition to a monoclinic phase (γ–Ce_3Al), space group $P112_1/m$ (No. 11), with $a = 6.824$ Å, $b = 12.458$ Å, $c = 5.366$ Å, and $\gamma_m = 89.69°$ (values at $T = 15$ K). There are two inequivalent Al sites, both in 2e Wyckoff position, and six inequivalent Ce sites, all in 2e, in the monoclinic unit cell. In both the hexagonal and the monoclinic structures, each atom lies on a mirror plane normal to the *z*–axis and has 12–fold coordination. Six neighbors are in the same plane, and three neighbors each are in the upper and lower planes.

The monoclinic structure is very close to orthorhombic, as the monoclinic angle $\gamma_m \sphericalangle\ a,\ b$ is very close to 90° and $b_{orth} \sim (3/2)^{-1/2} a_{hex}$. The monoclinic symmetry of the γ phase results from large shifts of atoms within the mirror planes from their more symmetric positions in the parent hexagonal α phase [6]. Close similarity of the α and γ structures is evident from comparison of projections of the two crystal structures along the *z*–axis (figures A1(a) and (b)), where for the α phase, both the hexagonal and the orthohexagonal unit cells are drawn. The lattice constants of the monoclinic cell nearly equal those of the orthohexagonal cell of the hexagonal phase. In figure A1(c), the monoclinic and the orthohexagonal cells are drawn superimposed on each other with the atomic shifts (from hexagonal to monoclinic) marked by arrows. The structure of the γ phase can be viewed as consisting of slightly tilted (zig–zag) Ce–Al and Ce–Ce chains (hence Ce_3Al) along the *a* direction, alternately stacked along both the *b* and the *c* directions (figure A1(d)). There are two types of the Ce–Ce chains, one

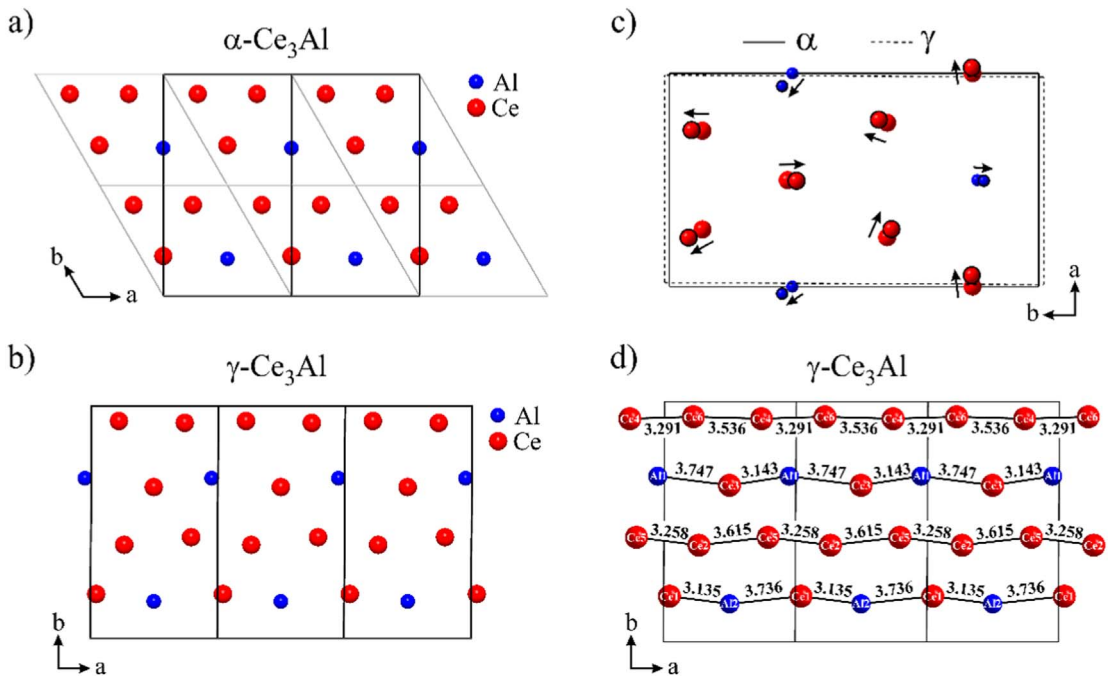

Figure A1. (a) Projection of the $\alpha-Ce_3Al$ hexagonal structure along the *z*–axis, where both the hexagonal and the orthohexagonal unit cells are drawn. (b) A projection of the $\gamma-Ce_3Al$ monoclinic structure along the *z*–axis. (c) The monoclinic (dashed frame) and the orthohexagonal (solid frame) cells superimposed on each other with the atomic shifts from the hexagonal to the monoclinic structure marked by arrows (atomic positions in the monoclinic unit cell are encircled black). (d) The structure of the γ phase can be viewed as consisting of slightly tilted Ce–Al and Ce–Ce chains along the *a* direction, alternately stacked along both the *b* and *c* directions.

composed of Ce(2) and Ce(5) and the other of Ce(4) and Ce(6). There exist also two different Ce–Al chains, one composed of Ce(3) and Al(1) and the other of Ce(1) and Al(2). On each of the chains, there are two alternating distances between the nearest neighbors, one 'short' and one 'long' (Ce(2)–Ce(5): 3.258 and 3.615 Å; Ce(4)–Ce(6): 3.291 and 3.536 Å; Ce(3)–Al(1): 3.143 and 3.747 Å; Ce(1)–Al(2): 3.135 and 3.736 Å). The distances are also indicated in the graph.

Appendix B. Material and methods

The Ce_3Al monocrystal was grown by the Czochralski technique, using the Oxypuller 05–03 apparatus, produced by Cyberstar S.A. (Echirolles, France). The melt was prepared from a prealloyed Ce_3Al ingot of 8 g mass, contained within an Al_2O_3 crucible. The atmosphere in the furnace was flowing argon at ambient pressure. A Ce_3Al crystal from former experiments was used as the seed, without any predetermined orientation. The pulling rate was set at 1.5 mm h^{-1}. The final crystal had a mass of 3.9 g and exhibited two grains along the cross section. Each grain was crystallographically oriented uniformly over the entire length of 20 mm, which implied that the boundary between the grains was located approximately in the middle of the crystal. The two grains were separated by cutting with a wire saw.

The XRD pattern of a Ce_3Al monocrystalline sample at room temperature is shown in figure B1. All peaks could be indexed to a hexagonal close packed (hcp) structure (space group $P6_3/mmc$) with the lattice parameters $a = 7.03$ Å and $c = 5.29$ Å, in agreement with the literature data [5]. Miller indices *hkl* are written on the diffraction peaks. Large intensity of the 0*k*0 reflections and the absence of most reflections with nonzero *l* support the monocrystalline nature of the sample. Good crystallinity is evident also from the selected area electron diffraction (SAED) pattern shown in the inset of figure B1.

Magnetic measurements were conducted in part using a Quantum Design MPMS XL–5 SQUID magnetometer equipped with a 5 T magnet and in part using a Quantum Design MPMS3 SQUID magnetometer equipped with a 7 T magnet, both operating down to 1.9 K temperature. The electrical resistivity, the magnetoresistance and the specific heat were measured with a Quantum Design Physical Property Measurement System (PPMS 9 T), equipped with a 9 T magnet and a ^{3}He cryostat, operating down to 0.35 K temperature.

For the magnetic susceptibility measurements, three needle–shaped samples of $4 \times 0.5 \times 0.5$ mm^3 dimensions were cut from the parent monocrystal with their long axes oriented parallel to the *a*, *b* and *c* directions of the low–temperature monoclinic phase. The electrical resistivity and the magnetoresistance

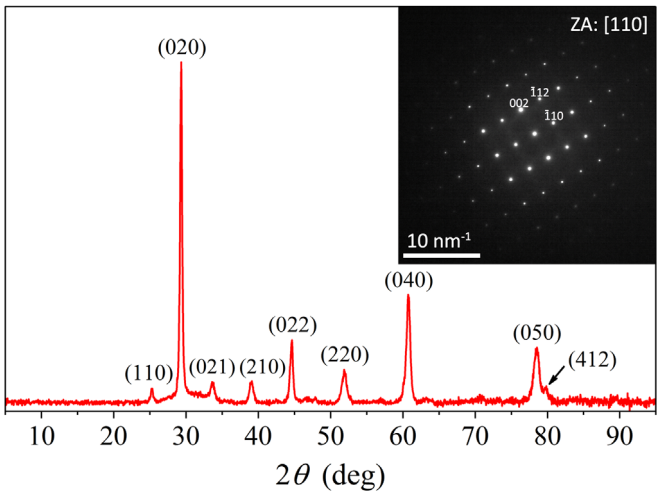

Figure B1. The XRD pattern of the Ce_3Al monocrystalline sample at room temperature (Cu $K_{\alpha 1}$ radiation, $\lambda = 1.54056$ Å). The inset shows SAED pattern taken in the [110] zone axis (ZA). Probe size for the electron diffraction was 7 nm.

experiments were conducted on a rectangular bar–shaped sample of $4 \times 1 \times 1$ mm^3 dimensions with its long axis parallel to *a*. The specific heat was measured on a cube–shaped sample of 1 mm edge length.

In our measurements of the physical properties of a Ce_3Al monocrystal in a magnetic field applied along the *a*, *b* and *c* crystallographic directions, we consistently found that the properties were close to isotropic for the field applied in the (*a*, *b*) monoclinic plane, whereas there was a large anisotropy to the properties for the field along *c*. This kind of anisotropy is similar to that found in hexagonal lattices [19], where at high temperatures, the basal plane is the easy plane of magnetization (magnetically isotropic). The orientation of the moments is determined by the product of the 4 *f* charge–density electric quadrupole moment and the electric field gradient at the RE site, which for the Ce^{3+} ions with oblate (flattened) charge density in a hexagonal field directs the moments into the basal plane. At low temperatures, the basal plane may become magnetically anisotropic with six equivalent easy directions at a 60° azimuthal angle to each other and the moments may also be somewhat pulled out of the basal plane. There, however, still exists large anisotropy to the perpendicular hexagonal direction. For the Ce_3Al, the reason for the hexagonal–like anisotropy in the low–temperature monoclinic phase is the structural similarity of this phase to the parent hexagonal phase, as described in the appendix A. The small anisotropy of the properties observed experimentally also in the (*a*, *b*) plane is considered to originate predominantly from the monoclinic distortion of the hexagonal symmetry, but such anisotropy is at low temperatures also inherent to the hexagonal phase. The experimental error due to small deviation of the applied field direction from the crystallographic axes (especially the tilt out of the monoclinic plane) could add to the effective anisotropy as well. Different tilts of the field away from the *c* axis are believed to be the main reason for the small difference between the $T_N^c(B)$ data points (figure 2(a)) determined from the magnetic susceptibility χ^c and the specific heat C^c.

The small discrepancy that the T_N values determined from the specific heat are systematically lower by 0.2 K as compared to the values determined from the magnetic susceptibility peak are very likely a consequence of the criterion for the T_N determination from χ. We used the temperature of the χ maximum as T_N, whereas another common definition of T_N is the temperature of the $d\chi/dT$ slope maximum that would yield a slightly lower value.

Appendix C. Anisotropic electrical resistivity in a magnetic field

To study the anisotropy of the electrical resistivity in a magnetic field, three sets of experiments were conducted, with the electric current always directed along the *a* direction (the direction of the Ce–Ce and Ce–Al atomic chains), whereas the magnetic field was applied along the *a*, *b* and *c* directions. The anisotropic resistivity is labeled by a superscript denoting the direction of the magnetic field, ρ^a, ρ^b, and ρ^c. The measurements were performed in the temperature range between 300 and 0.35 K in magnetic fields between 0 and 9 T in steps of $\Delta B = 1$ T.

The resistivities $\rho^{a,b,c}$ between 60 and 0.35 K are shown in figure C1. Their temperature dependence is typical of a Kondo–lattice system, by exhibiting a Kondo resistance minimum at $T_K \approx 23$ K and a maximum at the lattice Kondo temperature $T^* \approx 3$ K, followed by a rapid decrease upon $T \rightarrow 0$. The magnetic field

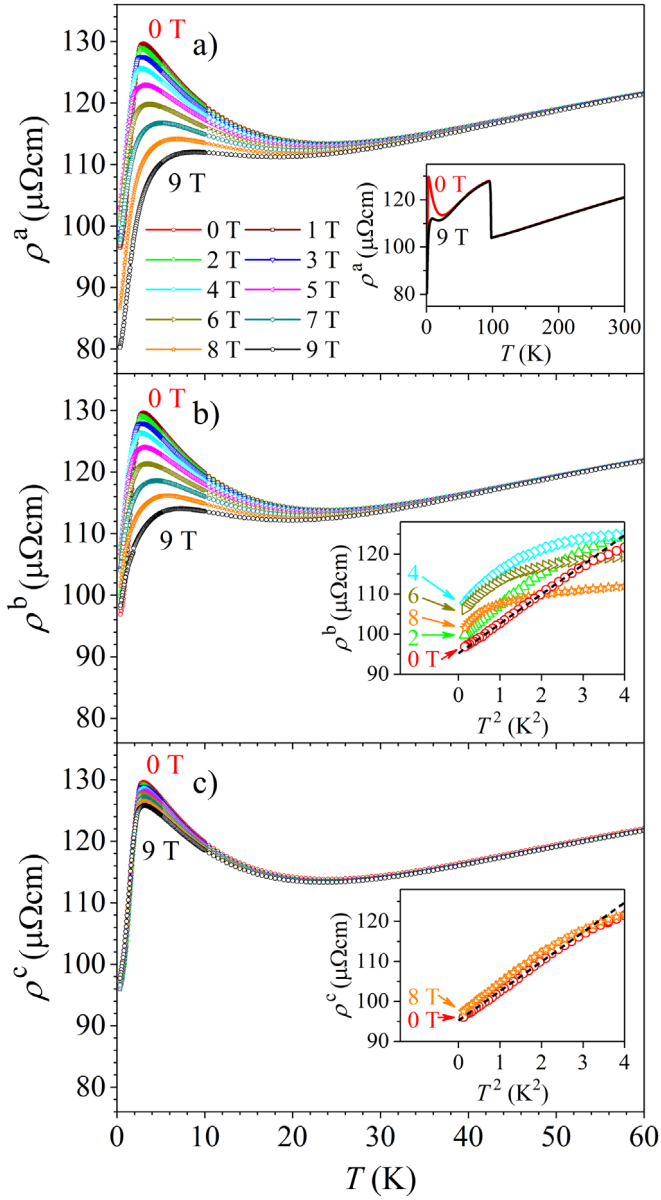

Figure C1. Electrical resistivity of the Ce_3Al in the temperature range between 60 and 0.35 K in magnetic fields 0–9 T for the current along the *a* direction and the field applied (a) along *a* direction (ρ^a), (b) along *b* direction (ρ^b) and (c) along *c* direction (ρ^c). The inset in panel (a) shows the resistivity ρ^a in the entire investigated temperature range (300–0.35 K) in two magnetic fields of 0 and 9 T. In the insets of panels (b) and (c), the $T \rightarrow 0$ resistivities ρ^b and ρ^c are plotted on a T^2 scale, respectively. Dashed line is the fit of the zero–field resistivity with the expression $\rho = \rho_{01} + \rho_1 T^2$ (with $\rho_{01} = 92\ \mu\Omega$cm and $\rho_1 = 6.8\ \mu\Omega\text{cm K}^{-2}$).

influences the resistivity below T_K in an anisotropic manner. While ρ^a and ρ^b are both significantly and almost equally affected by the field ($\rho^a \approx \rho^b$), the effect on ρ^c is much weaker. The resistivity ρ^a in the entire investigated temperature range (300–0.35 K) in two magnetic fields of 0 and 9 T is shown in the inset of figure C1(a). A sharp, discontinuous jump is observed at the $\alpha - \gamma$ structural phase transition (at $T \approx 100$ K). The electrical resistivity of Ce_3Al was investigated before on polycrystalline samples by various authors [7, 9–12]. Polycrystals show qualitatively similar features in the temperature–dependent resistivity (a jump at the $\alpha - \gamma$ transition, a minimum at T_K, a maximum at T^* and a strong drop below), but there exists some scatter of the temperature of the $\alpha - \gamma$ transition and of the T_K and T^* values between different samples. The resistivity values of polycrystalline samples also vary considerably. A pronounced difference between the polycrystals and our monocrystal is the resistivity step at the $\alpha - \gamma$ transition, which is truly discontinuous in the monocrystal, whereas it is more rounded (continuous–like) in polycrystals.

The resistivity of a Kondo–lattice system typically exhibits a $\rho \propto -\ln T$ behavior between T_K and T^*, corresponding to the regime of a single–impurity Kondo effect. For the Ce_3Al, such behavior was confirmed before on a polycrystalline sample [7] and since our results are in complete agreement, we do not repeat the analysis here. Below the lattice Kondo temperature T^*, the resistivity strongly drops, because scattering of the

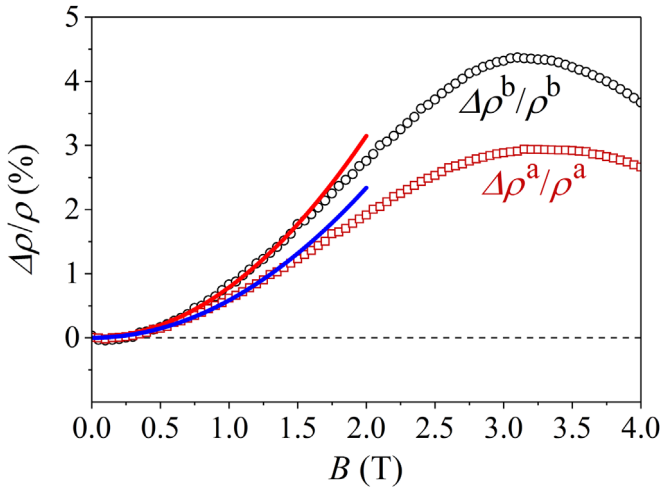

Figure C2. The 1.9-K curves of $\Delta\rho^a/\rho^a$ and $\Delta\rho^b/\rho^b$ on an expanded scale, with parabolic fits in the low–field region that demonstrate an AFM-type B^2–magnetoresistance up to about 1.5 T.

electrons on rare–earth ions arranged on a periodic sublattice becomes coherent. The lattice part of the resistivity becomes negligibly small and the scattering of the electrons by spin fluctuations from the Kondo ground state becomes dominant in the $T \rightarrow 0$ limit. Since the electronic term in the resistivity involves electron–electron scattering, this leads to a $\rho \propto T^2$ behavior, as expected from such a mechanism. The temperature dependence of the resistivities ρ^b and ρ^c in the $T \rightarrow 0$ limit is presented in the insets of figures C1(b) and (c), respectively, where the resistivity is plotted on a T^2 scale for 0.35 K $< T <$ 2 K in magnetic fields between 0 and 8 T. The zero–field resistivity shows a T^2 dependence up to $T \approx$ 1.7 K (or up to $T^2 \approx 3$ K^2), where the fit with the expression $\rho = \rho_{01} + \rho_1 T^2$ is shown by a dashed line (the values of the fit parameters are given in the figure caption). Upon increasing the magnetic field, the temperature interval where ρ^b shows a T^2 dependence becomes progressively smaller (the upper limit of this interval shifts to lower temperatures), whereas for fields $B >$ 4 T, no T^2 dependence can be claimed anymore (inset in figure C1(b)). For ρ^c, the T^2 dependence is affected by the magnetic field much less and persists up to the highest field (inset in figure C1(c)).

The electrical resistivity of the Ce_3Al in the monoclinic phase is predominantly determined by the Kondo effect on the Ce–Ce chains. Magnetic ordering on the Ce–Al chains starts to affect the resistivity below the Néel temperature $T_N = 2.6$ K, which is best observed in the magnetoresistance, as discussed in the main paper.

The B^2-dependence of the magnetoresistances $\Delta\rho^a/\rho^a$ and $\Delta\rho^b/\rho^b$ within the AFM phase in the low–field range (roughly in the interval $0 < B <$ 1.5 T) is demonstrated in figure C2, where the 1.9-K curves were fitted with a parabola, $\Delta\rho^i/\rho^i = A_i B^2$.

ORCID iDs

P Koželj https://orcid.org/0000-0001-9837-7516
J Dolinšek https://orcid.org/0000-0002-5750-802X

References

[1] See, for a review Sachdev S 1999 *Quantum Phase Transitions* (Cambridge: Cambridge University Press)
[2] See, for a review 2011 *Understanding Quantum Phase Transitions* Carr L D (ed) (Boca Raton: CRC Press, Taylor and Francis group)
[3] Si Q Quantum criticality and the Kondo Lattice in: *Understanding Quantum Phase Transitions* (Ref. [2]), Ch. 8 193–216
[4] Gegenwart P and Steglich F Probing quantum criticality and its relationship with superconductivity in heavy fermions in: *Understanding Quantum Phase Transitions* (Ref. [2]), Ch. 18 445–67
[5] Lawson A C, Lawrence J M, Thompson J D and Williams A 1990 *Low temperature crystal structure of Ce_3Al Physica B* **163** 587
[6] Sakurai J, Matsuura T and Komura Y 1988 *Transport and crystal properties of α– and β–Ce_3Al J. Phys. (Paris) Colloq.* **49** C8–783
[7] Singh D, Yadam S, Venkateshwarlu D, Gangrade M, Shanmukharao Samatham S and Ganesan V 2014 *Magnetic field driven quantum critical phase transition in Ce_3Al Mater. Res. Express* **1** 046114
[8] Li W-H, Peng J C, Lin Y-C, Lee K C, Lynn J W and Chen Y Y 1998 *Magnetic ordering of Ce in the heavy–fermion compound Ce_3Al J. Appl. Phys.* **83** 6426
[9] Chen Y Y, Yao Y D, Hu B C, Jang C H, Lawrence J M, Huang H and Li W H 1997 *Structure, crystal fields, magnetic interactions, and heavy–fermion behavior in $(Ce_{1-x}La_x)_3Al$ Phys. Rev. B* **55** 5937
[10] Sera M, Satoh T and Kasuya T 1987 *Magnetic and transport properties of Kondo compound α–Ce_3Al J. Magn. Magn. Mater.* **63&64** 82
[11] Thompson J D, Fisk Z, Chen Y-Y and Lawrence J M 1987 *Pressure investigation of the new Kondo lattice systems Ce_3Sn, Ce_3In and Ce_3Al J. Less–Common Met.* **127** 385

[12] Chen Y-Y, Lawrence J M, Thompson J D and Willis J O 1989 *Thermodynamic behavior of the heavy–fermion compounds Ce_3X ($X = Al$, In,Sn) Phys. Rev. B* **40** 10766
[13] Yamada H and Takada S 1972 Negative magnetoresistance of ferromagnetic metals due to spin fluctuations *Prog. Theor. Phys.* **48** 1828
[14] Yamada H and Takada S 1973 Magnetoresistance of antiferromagnetic metals due to s–d interaction *J. Phys. Soc. Jpn.* **34** 51
[15] Satoh K, Fujita T, Maeno Y, Ōnuki Y, Komatsubara T and Ohtsuka T 1985 *Anisotropic specific heat of $CeCu_6$ in magnetic fields Solid State Commun.* **56** 327
[16] Conduit G J, Green A G and Simons B D 2009 Inhomogeneous phase formation on the border of itinerant ferromagnetism *Phys. Rev. Lett.* **103** 207201
[17] Holtschneider M and Selke W 2008 Uniaxially anisotropic antiferromagnets in a field on a square lattice *Eur. Phys. J. B* **62** 147
[18] Coey J M D 2010 *Magnetism and Magnetic Materials* (Cambridge: Cambridge University Press) pp 196–9
[19] Coey J M D 2010 *Magnetism and Magnetic Materials* 170